Stripe-Width-Dependent Microstructural Evolution in Multifilamented $YBa_2Cu_3O_{7-\delta}$ Films Revealed by Cross-Sectional Analysis

Taiki Wada[a], Hiroki Fujimoto[a], Yasuhito Kawahara[a], Akiyoshi Matsumoto[b], Ryo Teranishi[a*]

[a] Department of Materials, Kyushu University, Fukuoka 819-0395, Japan

[b] National Institute for Materials Science, Tsukuba 305-0047, Japan

* Corresponding author: teranishi.ryo.438@m.kyushu-u.ac.jp

Abstract

Multifilamentation of $YBa_2Cu_3O_{7-\delta}$ (YBCO)-coated conductors with a continuous and as-narrow-as-possible gap layer is considered an important structural requirement for maximizing current-carrying performance and reducing alternating-current loss. This study aims to establish a microstructural design guideline for controlling the formation of continuous gap layers by clarifying the relationship between Nb stripe geometry and the resulting non-superconducting gap-layer structure. The effect of stripe width on the width of non-superconducting gap layers was systematically investigated by laser and electron microscopy. Laser microscopy revealed that the actual stripes widths were several micrometers larger than the designed values and that the stripe height increased with increasing stripe width. Microstructural analysis by electron microscopy showed that Ba and O diffused into Nb stripes, forming $Ba_5Nb_4O_{15}$. For the 1-µm stripe, Y–Cu–O and Cu–O phases, as well as the YBCO matrix, were present on the stripe. By contrast, for the 2-µm, 5-µm, and 10-µm stripes, a continuous non-superconducting layer composed of the Y–Cu–O and Cu–O phases were formed. The thickness of the non-superconducting layer increased with increasing Nb stripe width (i.e., volume), indicating that its formation is driven by $Ba_5Nb_4O_{15}$ formation. Among the stripe widths examined in the triple-coated YBCO thin films evaluated under the conditions of this study, the Nb stripe with a design width of 2 µm (actual width of 4.9 µm) achieved the narrowest continuous non-superconducting gap layer. These findings provide a microstructural

design guideline for designing bottom-up multifilamented YBCO-coated conductors with continuous and narrow gap layers.

Keywords:

Multifilamentation

$YBa_2Cu_3O_{7-\delta}$ superconducting film

Film growth

Cross-sectional TEM

Microstructure observations

1. Introduction

Superconductivity is characterized by zero electrical resistance and perfect diamagnetism below a critical temperature, enabling a wide range of applications including magnetic levitation, high-field magnets, magnetic resonance imaging, and electric power devices. For example, rare-earth-based bulk superconductors such as (RE)BCO-358 have demonstrated excellent levitation performance and attractive electromagnetic properties [1,2]. Among the various superconducting materials, $REBa_2Cu_3O_{7-\delta}$ (RE: Rare Earth, REBCO) coated conductors (CCs) have attracted particular attention because of their high critical current density under strong magnetic fields and their potential for applications in fusion reactors, high-field magnets, and electric power technologies [3,4]. REBCO CCs are high-temperature superconductors with a triple perovskite structure and are expected to find practical application in superconducting coils and magnets for power applications and high-magnetic-field generation [4–8]. Such coils and magnets are promising candidates for use in future nuclear fusion reactors and NMR systems requiring high magnetic fields. However, their practical implementation is hindered by alternating-current (AC) loss, which is generated under time-varying currents and magnetic fields [9–13]. This loss originates from the motion of magnetic flux penetrating the REBCO CCs, driven by the Lorentz force, resulting in energy dissipation. To address this issue, multifilamentation has been employed to reduce AC losses by introducing non-superconducting gap layers into the REBCO CCs. Dividing the conductor into N filaments shortens the migration distance of magnetic flux, decreasing the AC loss by a factor of approximately 1/N [14–16]. However, the geometry of the gap layer is also critical for practical applications. A continuous gap layer is required to electrically isolate adjacent superconducting filaments and suppress coupling currents, whereas an excessively wide gap decreases the superconducting cross-sectional area, leading to deterioration of the current-carrying capability. Therefore, optimizing the gap-layer width is essential for balancing AC-loss reduction and transport performance.

Various techniques for multifilamentation have been proposed to date [14–18]. Top-down approaches such as laser scribing have been widely investigated for dividing the superconducting layer [19–23]. In contrast, bottom-up approaches such as inkjet printing have also been developed to directly deposit patterned structures [24–27]. However, these conventional methods face specific challenges. For instance, laser scribing can induce local heat damage in the superconducting layers [19–23]. Meanwhile, inkjet printing typically results in relatively large gap widths on the order of several tens of µm, which leads to a reduction in the current-carrying capacity per unit width of the superconducting wire [24–27].

To address the issue of thermal damage caused by laser irradiation and to enable finer gap widths, a bottom-up multifilamentation method based on photolithography was developed in this study, involving the patterning of metallic (e.g., Zr or Nb) stripes on the substrate prior to REBCO deposition [28–32]. Compared to conventional techniques, this method enabled the formation of layers with extremely narrow gaps (of the order of a few µm) without causing heat damage by laser to the REBCO layer. In our previous studies [30–32], the formation mechanism of the gap layer was investigated based on cross-sectional scanning transmission electron microscopy (STEM) observations. These studies revealed that Nb stripes react with BaO, a precursor component of $YBa_2Cu_3O_{7-\delta}$ (YBCO), leading to local compositional deviation on the stripes and the formation of non-superconducting phases like Y-Cu-O and Cu-O [33]. This outcome indicates that the size of the non-superconducting region can be controlled by the absolute amount of Nb that reacts with BaO in principle. For the practical application of bottom-up multifilamented REBCO CCSs fabricated using the proposed method, continuous and narrow non-superconducting gap layers are considered an important structural requirement for reducing AC loss while maintaining current-carrying capability. Consequently, establishing structural design guidelines to control the width and continuity of these non-superconducting gap layers is essential.

Therefore, the objective of this study is to establish a quantitative microstructural design guideline for controlling the formation, width, and continuity of non-superconducting gap layers in bottom-up multifilamented REBCO coated conductors. Building on our previous study [33], which clarified the formation mechanism of non-superconducting phases, this work extends the investigation from two representative stripe widths (1 and 10 μm) to a systematic evaluation over the entire width range by including intermediate widths of 2 and 5 μm. Combined with a quantitative volumetric analysis of the non-superconducting phases, this systematic investigation clarifies how Nb stripe geometry governs gap-layer formation and provides practical structural design guidelines for achieving continuous and as-narrow-as-possible non-superconducting gap layers.

2. Experimental Methods

2.1 Sample preparation

A YBCO thin film with Nb stripes was prepared as described below. Nb was selected as the stripe material owing to its strong reactivity with BaO.

First, a photoresist (OFPR700LB, Tokyo Ohka Kogyo Co., Ltd.) was coated onto a 5×5 mm^2 $SrTiO_3$ (STO) single-crystal substrate. The photoresist was then patterned into longitudinal stripes using a maskless lithography system (DL-1000, Nano System Solutions Corporation). Following exposure, the substrate was developed using tetramethylammonium hydroxide to remove the ultraviolet-exposed regions. Subsequently, a thin Nb film was deposited onto the patterned substrate at approximately 25 ℃ via a DC magnetron sputtering system (CFD-4EP-LL (4G), Shibaura Mechatronics Co., Ltd.). Finally, the remaining photoresist was removed using a solvent lift-off process. This procedure yielded four longitudinally aligned Nb stripes with widths of 1, 2, 5, and 10 μm. The corresponding Nb-striped substrates are hereafter referred to as Nb-1, Nb-2, Nb-5, and Nb-10. The fabrication process and the Nb-striped substrate are schematically shown in Fig. 1.

Subsequently, a YBCO thin film was fabricated on the patterned substrate using the trifluoroacetic acid metal-organic deposition (TFA-MOD) method. The heat-treatment process for YBCO crystallization involved in the TFA-MOD method is illustrated in Fig. 2. The MOD precursor solution was prepared by dissolving Y_2O_3 and BaO in trifluoroacetic acid and CuO in 2-ethylhexanoic acid, followed by mixing the two organic solutions in 1-methoxy-2-propanol to obtain a concentration of 1.1 M. The molar ratio of Y:Ba:Cu was set at 1:1.5:3. During the YBCO film deposition process, the precursor solution was dropped onto the substrate and spin-coated at 3000 rpm for 2 min. The coated substrate was calcined at 430 °C under a pure oxygen atmosphere to form a precursor film. These coating and calcination processes were repeated three times. The calcined sample was then crystallized at 780 °C in a 0.1% O_2/Ar atmosphere, followed by oxygen annealing at 450 °C. For comparison of X-ray diffraction (XRD) patterns, a YBCO thin film was also fabricated under identical coating and heat-treatment conditions on the STO substrate without Nb stripes. XRD analyses of these samples were performed to evaluate the influence of Nb stripes on YBCO phase formation.

2.2 Analysis methods

The surface profiles including the widths and heights of the Nb stripes were evaluated using a laser confocal microscope (OLS4500, Olympus). The measurements were performed using a 405 nm semiconductor laser as the light source. XRD analyses of the YBCO-deposited surfaces were carried out using a Cu-Kα radiation source operated at 30 kV and 30 mA with a RINT2200HF (Rigaku, Japan) instrument. Secondary-electron (SE) SEM images were acquired from the deposited surfaces using an Ultra55 equipped with a field-emission gun and operated at 10–15 kV. The working distance for SE-SEM imaging was set to 8.5 mm. Thin-foil specimens for transmission electron microscopy (TEM) were prepared by a focused ion beam (FIB) lift-out method using an FEI Helios 5 UX dual-beam instrument. Bright-field TEM (BF-TEM) images, selected-area electron diffraction pattern (SAEDp), and STEM observations were performed using a JEM-ARM200CF (JEOL, Japan) instrument equipped with a cold field-emission gun and a spherical aberration corrector (CEOS, Germany), operated at 200 kV. High-angle annular dark-field (HAADF)-STEM images with a collection semi-angle of 52–148 mrad and a convergence semi-angle of 25 mrad were used for cross-sectional characterization. Elemental distribution maps were acquired by energy-dispersive X-ray spectroscopy (EDS) using a twin silicon drift detector (SDD) with a collection solid angle of 2.0 sr (Centurio Large Angle SDD-EDS, JEOL, Japan).

2.3 Magnetic characterization

Magneto-optical imaging (MOI) was additionally employed to evaluate the superconducting properties of the fabricated samples. The superconducting transition temperature (T_c) was estimated from the temperature at which magnetic flux exclusion became observable during cooling under an applied magnetic field.

To provide a preliminary magnetic assessment of the current-carrying capability, the local critical current density (J_c) was estimated from the magnetic-flux-density gradients obtained from calibrated MOI images using the Bean critical-state model. Magnetic-flux-density profiles were extracted across the regions between adjacent Nb stripes, where continuous non-superconducting gap layers were formed, and the corresponding local field gradients were analyzed to estimate J_c. The obtained T_c and J_c values represent magnetic estimates derived from MOI observations and should not be interpreted as direct electrical transport measurements.

3 Results and discussion

3.1 Laser microscopy characterizations of STO substrates with Nb stripes

Prior to YBCO deposition, the widths and heights of four Nb stripes patterned on the STO substrates were measured via laser microscopy. Fig. 3 shows SEM micrographs of the Nb-striped STO substrates and their corresponding height profiles extracted along the regions indicated by the red lines in their micrographs. The images confirm that the Nb stripes were uniformly formed on the STO substrate.

As shown in the height profiles in Fig. 3, peaks were observed at the stripe edges, which are attributed to system-related artifacts of the laser microscopy. For regions affected by these system-induced artifacts, the stripe height was evaluated as the height difference between the average height of the stripe region excluding the artifact-affected areas and that of the substrate used as the reference region. The measured stripe heights are indicated by the blue lines in Fig. 3.

The measured stripe widths and heights are summarized in Table 1, which shows that the patterned stripe widths are several μm larger than the designed values. This is a typical feature of photolithography, attributed to diffraction of ultraviolet light during exposure, which broadens the openings of the photoresist mask [34]. Additionally, although the stripe height was designed to be constant, the stripe height increased with increasing stripe width, also attributed to the photolithographic process. During Nb sputtering into the photoresist grooves, narrower grooves hinder uniform Nb deposition owing to shadowing near the groove openings, resulting in insufficient Nb accumulation. As a result, it is considered that the amount of Nb deposited was insufficient for the narrow stripes, and the stripe height after lift-off did not reach the design value.

3.2 XRD characterizations of YBCO thin films without and with Nb stripes

As a baseline, Fig. 4 shows the θ-2θ results obtained from XRD patterns of the fabricated YBCO thin films, which are reproduced from our previous publication [33]. Figs. 4(a) and 4(b) correspond to YBCO thin films without and with Nb stripes, respectively. In both patterns, diffraction peaks corresponding to c-axis-oriented YBCO are clearly observed, together with peaks assigned to secondary phases of Ba_2CuO_3, as well as YBCO precursor phases including CuO and $Y_2Cu_2O_5$. However, Y_2BaCuO_5 only observed in the sample without stripes, indicates the preferential diffusion of Ba into the Nb stripes during the heat treatment in Fig. 4(a). No diffraction peaks attributable to the Nb stripes can be detected in Fig. 4(b). This absence is attributed to the extremely small volume fraction of Nb stripes within the films (estimated to be approximately 0.2%), which is below the detection limit of the XRD analyses.

3.3 SEM micrograph characterizations of the YBCO thin films with Nb stripes

Figs. 5(a–d) show SE-SEM images of the Nb-1, Nb-2, Nb-5, and Nb-10 samples, respectively. As indicated by the red arrows in the images, linear dark contrasts are confirmed across the entire field of view. The width of these linear dark contrasts increases with increasing stripe width, indicating that they originate from the Nb stripes. Additionally, cracks are observed on the stripes, as highlighted by the yellow circles in Figs. 5(b), (c), and (d). The formation of larger cracks is more pronounced with increasing stripe width.

Figs. 6(a–d) show elemental distribution maps of the Nb-1, Nb-2, Nb-5, and Nb-10 samples, respectively, obtained via SEM-EDS analysis. The elemental maps revealed that the matrix regions are uniformly composed of Y–Ba–Cu–O, based on the XRD results shown in Fig. 4, it was confirmed that YBCO is formed in these regions. Along the linear contrasts attributed to the stripes, the presence of Y, Cu, O, and Nb, accompanied by Ba depletion, is clearly observed. In particular, Cu and Nb enrichment is detected in Figs. 6(a) and (b), whereas enrichment of Y, Cu, and Nb is observed in Figs. 6(c) and (d). Furthermore, as shown in Figs. 6(b), (c), and (d), Ba–Nb–O is detected in the cracks on the stripes, whereas Y and Cu are depleted in these regions. This result indicates that Ba on the stripes diffused into the underlying Nb during heat treatment, resulting in the formation of Y–Cu–O and Cu–O phases on the stripes.

The widths of the Y- and Cu-enriched, Ba-depleted regions, and Nb-enriched regions in Figs. 6(a) to (d) are indicated by yellow and red arrows. As shown by the yellow arrows in Figs. 6(c) and (d), the widths of the Y- and Cu-enriched regions coincide with those of the Ba-depleted regions. Overall, the widths indicated by the yellow arrows increase as the Nb-containing regions (or Nb stripes) become wider (red arrows). This trend suggests that the amount of Ba diffusing from the matrix into the Nb stripes increases with increasing stripe width.

Additionally, comparison with laser microscopy measurements of stripe widths before heat treatment reveals that the stripe widths remain nearly unchanged upon heat treatment.

Furthermore, with increasing stripe width and height, large cracks, highlighted by the yellow circles in Figs. 5(b), (c), and (d), were formed on the stripes exclusively in the Y–Cu–O and Cu–O phases. This suggests that these cracks originate from thermal contraction of the Y–Cu–O and Cu–O phases. With increasing stripe height, the curvature of the non-superconducting phases on the stripes increased, thereby increasing surface stress. Consequently, enhanced thermal stress was applied during thermal expansion and shrinkage, which resulted in crack formation.

3.4 Cross-sectional STEM characterizations of the YBCO thin film with Nb stripes

Figs. 7(a–d) show HAADF-STEM images of the Nb-1, Nb-2, Nb-5, and Nb-10 samples, respectively (Nb-1 and Nb-10 micrographs were reproduced from our previous work [33]). In the Nb-1 sample, several granular contrasts, which are considered to be non-superconducting phases, are observed in the vicinity of the stripe. By contrast, in the Nb-2, Nb-5, and Nb-10 samples, a uniform contrast extending smoothly from directly above the stripe toward the stripe edges, attributed to a non-superconducting layer, can be observed. As indicated by the red double arrows, the width of the non-superconducting layer increases with increasing stripe width. These non-superconducting layers are adjacent to the YBCO matrix formed on the STO substrate. Additionally, for the Nb-5 and Nb-10 samples, layered voids are observed at the interface between the non-superconducting phases on the stripes and the stripes themselves. Moreover, void formation within the stripes can be observed in all the samples.

For each sample, the maximum stripe height, thickness of the overlying film on the stripe, and thickness of the YBCO film on the STO substrate are summarized in Table 2. The results revealed that neither the thickness of the non-superconducting layer on the stripe nor that of the YBCO film on the STO substrate depends on the stripe width or height. Additionally, in contrast to the stripe width, the stripe height increases significantly after the heat-treatment process compared to that before heat treatment.

Fig. 8 presents the elemental distribution maps obtained by STEM-EDS analysis. In all samples, Ba and O were completely diffused into the Nb stripes, confirming the formation of Ba–Nb–O compounds. From the elemental distribution maps, it is evident that BaO, a precursor of YBCO, diffused deeply into the stripes and reacted with Nb to form Ba–Nb–O compounds.

Because Ba diffuses into the Nb stripe much faster than Nb diffuses outward, the interdiffusion process is highly unbalanced, resulting in a net vacancy flux toward the interface. Such asymmetric interdiffusion and the associated vacancy accumulation are known to cause Kirkendall void formation [35]. Therefore, the layered voids observed at the interface in Nb-5 and Nb-10 samples are considered to be Kirkendall voids. Additionally, the voids formed within the stripes observed in all samples are attributed to vacancy diffusion induced by the Kirkendall effect and volumetric expansion of the stripe material during Ba–Nb–O formation [35]. Moreover, Ba–Nb–O compounds were identified as polycrystalline $Ba_5Nb_4O_{15}$ in the Nb-1 and Nb-10 samples based on previous literature [33].

Fig. 9 shows the BF-TEM images and SAEDp. The regions indicated by red circles in the BF-TEM images in Fig. 9(a) correspond to those marked by red circles in the HAADF-STEM images (Figs. 7(b) and (c)) and the SAEDp (Fig. 9(b)) are obtained from these regions. The SAEDp acquired from the stripe regions in the Nb-2 and Nb-5 samples are also consistent with the polycrystalline ring patterns of $Ba_5Nb_4O_{15}$, similar to those observed in the Nb-1 and Nb-10 samples. The increase in stripe height is attributed to the volumetric expansion associated with the chemical reaction of Nb to $Ba_5Nb_4O_{15}$. In the lateral direction, this volumetric expansion is strongly constrained by the surrounding YBCO matrix, whereas in the vertical direction, the constraint imposed by the overlying thin film is relatively small. Consequently, the volumetric expansion preferentially occurs in the stripe height direction, leading to a significant increase in stripe height upon heat treatment.

Furthermore, elemental mapping of the blue-boxed region in the HAADF-STEM image of the Nb-1 sample reveals the presence of Y–Cu–O and Cu–O phases in the YBCO matrix on the stripe. By contrast, the elemental maps of the Nb-2, Nb-5, and Nb-10 samples show complete Ba depletion on the stripes, indicating the absence of the YBCO matrix and the formation of a complete non-superconducting gap layer, composed of Y–Cu–O and Cu–O phases. Moreover, the lateral extent of the Ba-depleted region increases with increasing stripe width, coinciding with the non-superconducting layer width. This result indicates that the formation of the non-superconducting layer is driven by the formation of $Ba_5Nb_4O_{15}$, and therefore, the width of the non-superconducting layer increases with increasing Nb stripe volume. The volumes of the continuous non-superconducting phases formed on the stripes were estimated for the Nb-2, Nb-5, and Nb-10 samples, employing the following two reactions:

$$1/2\ Y_2Cu_2O_5 + 2BaO + 2CuO \rightarrow YBa_2Cu_3O_{7-\delta} \quad (1)$$

$$5BaO + 2Nb_2O_5 \rightarrow Ba_5Nb_4O_{15} \quad (2)$$

Reactions (1) and (2) represent the typical formation reactions of YBCO via the MOD process and $Ba_5Nb_4O_{15}$, respectively [33,36,37]. First, the volume of $Ba_5Nb_4O_{15}$ was measured from the HAADF-STEM images, and the corresponding amount of substance was calculated using the molar volume of $Ba_5Nb_4O_{15}$ obtained from the Materials Project [38,39]. Subsequently, the BaO consumption calculated from Eq. (2) was used to estimate the $Y_2Cu_2O_5$ and CuO volumes that remained unreacted in Eq. (1), corresponding to the non-superconducting phases, based on their molar volumes obtained from the Materials Project [38–41]. The estimated volumes of the non-superconducting phases formed on the stripes were compared with those directly measured from HAADF-STEM images of the Nb-2, Nb-5, and Nb-10 samples, and the results are summarized in Table 3, which shows good agreement between the estimated and measured values, indicating that the volume of the non-superconducting phases on the stripes can be reasonably calculated using $Ba_5Nb_4O_{15}$ as an indicator. Furthermore, as the volumetric expansion of the Nb stripe prior to the reaction can predict the $Ba_5Nb_4O_{15}$ volume, the extent of the non-superconducting phase formed on the stripes can be controlled by identifying the BaO reaction products for other stripe materials as well. These results demonstrate that the gap-layer width can be rationally designed by controlling the stripe geometry and the amount of Ba consumed through the reaction, providing a practical design strategy for bottom-up multifilamented REBCO conductors.

From the REBCO multifilamentation perspective, the gap layer (non-superconducting layer) should be as narrow as possible to effectively reduce AC losses while still forming a complete non-superconducting region [18]. Based on the present experimental conditions, the Nb-2 sample (actual width: 4.9 µm) provided the narrowest continuous gap layer among the samples. However, since the Nb-1 sample (actual width: 3.4 µm) exhibited a discontinuous structure, the true threshold width required to achieve a continuous non-superconducting layer lies somewhere between 3.4 µm and 4.9 µm. Precisely identifying this intermediate critical width remains a crucial task for further minimizing the gap layer. These STEM results were in good agreement with the SEM observations, supporting the uniform formation of the cross-sectional microstructures.

Figure 10 shows magneto-optical imaging (MOI) of YBCO thin films with stripes, measured at 10 K under a magnetic field of 40 Oe; here, brighter contrast indicates higher magnetic flux density. The absence of sharp corners in the sample images is due to a trimming process performed prior to MO observation. During sample preparation, spin-coating the precursor solution causes liquid accumulation at the substrate corners, resulting in raised film areas after the crystallization heat treatment; since observing the sample in this state would lead to non-uniform film thickness and reduced image contrast, the samples were trimmed. While almost no bright contrast regions were observed in (a) Nb-1, band-like regions of bright contrast corresponding to magnetic flux penetration along the stripes were clearly observed in (b) Nb-2, (c) Nb-5, and (d) Nb-10. The lack of bright contrast regions in (a) Nb-1 can be attributed to the following: the stripes in Nb-1 appear discontinuous (as seen in Fig. 5(a)), and microstructural analysis (Figs. 7(a) and 8(a)) suggests YBCO formation on the stripes. These observations imply that the Nb layer was not continuously deposited across the substrate from edge to edge, or that the YBCO film formed on the stripes so that the area was not rendered completely non-superconducting. On the other hand, the results in (b) Nb-2, (c) Nb-5, and (d) Nb-10 revealed that magnetic flux penetrated independently into each filament separated by the continuous non-superconducting gap layers. This behavior indicates effective magnetic and electrical isolation between adjacent superconducting filaments. Such filament separation is expected to suppress electromagnetic coupling and therefore has the potential to reduce coupling-current-related AC losses in practical applications. This observation provides experimental support for the electrical isolation achieved by the proposed bottom-up multifilamentation process.

To provide a preliminary magnetic assessment of the fabricated samples, the superconducting properties were evaluated by the results of MOI. Magnetic flux exclusion became observable at approximately 89.0 K, which was taken as the estimated T_c. Furthermore, the local J_c, estimated from the magnetic-flux-density gradients using the Bean critical-state model, was approximately 6.6×10^4 Acm^{-2} at 10 K. Although these values were obtained from magnetic measurements rather than direct transport measurements, they confirm that superconductivity was maintained after introducing the Nb stripe structures. These magnetic evaluations were performed solely to confirm that superconductivity was preserved in the fabricated samples and were not intended as a systematic evaluation of electrical transport performance.

Among the Nb stripe widths investigated in this study, the designed stripe width of 2 μm (actual width: 4.9 μm) produced the narrowest continuous non-superconducting gap layer. This result indicates that a continuous gap layer can be achieved without unnecessarily increasing the non-superconducting region, thereby providing an appropriate balance between filament separation and retention of the superconducting cross-sectional area.

To further clarify the significance of the present results, Table 4 summarizes representative multifilamentation techniques reported in the literature and compares them with the present photolithography-based bottom-up approach. It compares the method used in this study with the laser scribing and inkjet printing methods—representative top-down and bottom-up approaches, respectively. This comparison covers processing principles, typical gap widths, advantages, limitations, and potential impacts on the superconducting layer. As summarized in Table 4, top-down techniques such as laser scribing can produce relatively narrow gap widths; however, they inevitably introduce heat-affected zones that may degrade the superconducting properties of the adjacent REBCO layer. In contrast, bottom-up techniques based on inkjet printing avoid thermal damage because the superconducting layer is deposited after patterning. Nevertheless, the limitation of nozzle size and the spreading of liquid inks after droplet landing generally results in relatively wide gap layers, reducing the effective superconducting cross-sectional area available for current transport. The photolithography-based approach employed in the present study combines the advantages of these two methods by producing a continuous gap layer with an actual width of only 4.9 μm while avoiding direct thermal processing of the superconducting layer.

More importantly, the contribution of the present work is not limited to demonstrating a narrow gap layer. By systematically correlating Nb stripe geometry with the formation and width of the non-superconducting gap layer through quantitative microstructural analysis, this study establishes a practical structural design guideline for bottom-up multifilamented REBCO coated conductors. Such a design guideline has not been presented in our previous work, which focused primarily on the formation mechanism of the non-superconducting phases, and provides a useful basis for future optimization of multifilament architectures.

This result indicates that a continuous gap layer can be achieved without unnecessarily increasing the non-superconducting region, thereby providing a practical structural design guideline for future bottom-up multifilamented REBCO coated conductors.

4. Conclusions

In this study, a multifilamented YBCO thin film was fabricated via the TFA-MOD method on an STO substrate patterned with Nb stripes of different widths using photolithography, and the influence of stripe width on the formation of non-superconducting gap layers was systematically investigated by laser microscopy and electron microscopy. For samples with designed stripe widths of 1, 2, 5, and 10 μm, the actual stripe widths were consistently several micrometers larger than the designed values, and the stripe height increased with increasing stripe width. Diffusion of Ba and O into Nb stripes indicated the formation of $Ba_5Nb_4O_{15}$ within the stripes. While the 1-μm stripe sample contained coexisting YBCO, Y–Cu–O and Cu–O phases on the stripe, continuous non-superconducting layers composed of Y–Cu–O and Cu–O phases were formed for the 2-, 5-, and 10-μm stripe samples. The width of the non-superconducting gap layer increased with increasing stripe width, indicating that its formation is governed by the reaction between Nb and Ba to form $Ba_5Nb_4O_{15}$.

Among the stripe widths investigated in the present triple-coated YBCO thin films, the Nb stripe with a designed width of 2 μm (actual width: 4.9 μm) produced the narrowest continuous non-superconducting gap layer. More importantly, this study establishes a quantitative relationship between Nb stripe geometry and gap-layer formation, providing a practical microstructural design guideline for controlling the width and continuity of non-superconducting gap layers in bottom-up multifilamented YBCO coated conductors. Although the present study focuses on the microstructural aspects, the proposed design guideline will be further validated through transport critical current and AC-loss measurements in future work.

Glossary

BF	Bright field
EDS	Energy-dispersive X-ray spectroscopy
HAADF	High-angle annular dark-field
MOD	Metal–organic deposition
REBCO	$REBa_2Cu_3O_{7-\delta}$
STEM	Scanning transmission electron microscopy
TFA	Trifluoroacetate
YBCO	$YBa_2Cu_3O_{7-\delta}$
XRD	X-ray diffraction

Fundings

This work was supported in part by JSPS KAKENHI under Grant 22H02019, and in part by the Joint Research Hub Program of the National Institute for Materials Science, Japan, and in part by the Ultra-microscopy Research Center of Kyushu University, Japan.

Data statement

All data that supports the findings of this study are included within the article.

Acknowledgments

This work was supported in part by the Joint Research Hub Program of the National Institute for Materials Science, Japan. Microstructural observations were carried out at the Ultra-microscopy Research Center (URC), Kyushu University, Japan.

Author contributions: CrediT

Taiki Wada: Methodology, Investigation, Data curation, Formal analysis, Visualization, Writing – original draft.

Hiroki Fujimoto: Investigation, Data curation, Visualization.

Yasuhito Kawahara: Data curation, Visualization, Formal analysis

Akiyoshi Matsumoto: Conceptualization, Writing – review & editing

Ryo Teranishi: Conceptualization, Supervision, Writing – review & editing, Funding acquisition.

References

[1] Sezai Kutuk, Suleyman Bolat, "Analysis of structural, electrical, and levitation properties of (RE: Nd, Sm, Gd) BCO-358 superconducting ceramics prepared by a modified MPMG technique", Journal of Materials Science, Volume 57, pages 1198–1214 (2022), 10.1007/s10853-021-06697-1

[2] Sezai Kütük, Süleyman Bolat,"Levitation Force of (RE)BCO-358 Bulk Superconductors", AIP Conference Proceedings, Vol. 2042 (2018), 10.1063/1.5078905

[3] Judith L. MacManus-Driscoll & Stuart C. Wimbush, "Processing and application of high-temperature superconducting coated conductors", Nature Reviews Materials volume 6, pages587–604 (2021),https://doi.org/10.1038/s41578-021-00290-3

[4] Li X, Ainslie M, Song D, Yang W and Macián-Juan R. REBCO coated conductors: Enabling the next generation of Tokamak reactors. Superconductor Science and Technology 2025;38(3);033001. https://doi.org/10.1088/1361-6668/ada9d2.

[5] Uglietti D. A review of commercial high temperature superconducting materials for large magnets: From wires and tapes to cables and conductors. Superconductor Science and Technology 2019;32(5);053001. https://doi.org/10.1088/1361-6668/ab06a2.

[6] Wang K, Dong H, Huang D, Shang H, Xie B, Zou Q, et al. Advances in second-generation high-temperature superconducting tapes and their applications in high-field magnets. Soft Science 2022;2(3);12. http://dx.doi.org/10.20517/ss.2022.10.

[7] Nagaya S, Watanabe T, Tamada T, Naruse M, Kashima N, Katagiri T, et al. Development of high strength pancake coil with stress controlling structure by REBCO coated conductor. IEEE Transactions on Applied Superconductivity 2013;23(3);4601204. http://dx.doi.org/10.1109/TASC.2012.2233854.

[8] Paidpilli M and Selvamanickam V. Development of RE-Ba-Cu-O superconductors in the U.S. for ultra-high field magnets. Superconductor Science and Technology 2022;35(4);043001. http://dx.doi.org/10.1088/1361-6668/ac5162.

[9] Coombs TA, Wang Q, Shah A, Hu J, Hao L, Patel I, et al. High-temperature superconductors and their large-scale applications. Nature Reviews Electrical Engineering 2024;1(12);788–801. https://doi.org/10.1038/s44287-024-00112-y.

[10] Pardo E, Šouc J and Kováč J. AC loss in ReBCO pancake coils and stacks of them: Modelling and measurement. Superconductor Science and Technology 2012;25(3);035003. http://dx.doi.org/10.1088/0953-2048/25/3/035003.

[11] Shiohara Y, Yoshizumi M, Takagi Y and Izumi T. Future prospects of high Tc superconductors-coated conductors and their applications. Physica C 2013;484;1–5. https://doi.org/10.1016/j.physc.2012.03.058.

[12] Ainslie MD. Reducing AC losses in high-temperature superconducting coated-conductor wires towards more efficient superconducting electric power applications. Superconductor Science and Technology 2019;32(3);030501. https://doi.org/10.1088/1361-6668/aafc40.

[13] Maeda H and Yanagisawa Y. Recent developments in high-temperature superconducting magnet technology (review). IEEE Transactions on Applied Superconductivity 2014;24(3);1–12. https://doi.org/10.1109/TASC.2013.2287707.

[14] Amemiya N, Kasai S, Yoda K, Jiang Z, Levin GA, Barnes PN, et al. AC loss reduction of YBCO coated conductors by multifilamentary structure. Superconductor Science and Technology 2004;17(12);1464–71. https://doi.org/10.1088/0953-2048/17/12/018.

[15] Grilli F and Kario A. How filaments can reduce AC losses in HTS coated conductors: A review. Superconductor Science and Technology 2016;29(8);083002. https://doi.org/10.1088/0953-2048/29/8/083002.

[16] Herrmann J, Müller K-H, Savvides N, Gnanarajan S, Thorley A and Katsaros A. A. Katsaros, AC losses of YBCO strips on YSZ/Hastelloy substrates. Physica C 2000;341–348;2493–4. https://doi.org/10.1016/S0921-4534(00)01284-3.

[17] Skarba M, Pekarčíková M, Frolek L, Cuninková E, Necpal M and Šimon Š. Striating of REBCO-coated conductors for AC loss reduction. IEEE Transactions on Applied Superconductivity 2023;33(9);1–6. https://doi.org/10.1109/TASC.2023.3327966.

[18] Wulff AC, Abrahamsen AB and Insinga AR. Multifilamentary coated conductors for ultra-high magnetic field applications. Superconductor Science and Technology 2021;34(5);053003. https://doi.org/10.1088/1361-6668/abee2b.

[19] Demeňcík E, Vojeňciak M, Kario A, Nast R, Jung A, Goldacker W, et al. AC loss and coupling currents in YBCO coated conductors with varying number of filaments. IEEE Transactions on Applied Superconductivity 2014;24(6);1–8. https://doi.org/10.1109/TASC.2014.2338320.

[20] Vojenčiak M, Kario A, Ringsdorf B, Nast R, van der Laan DC, Scheiter J, et al. Magnetization ac loss reduction in HTS CORC® cables made of striated coated conductors. Superconductor Science and Technology 2015;28(10);104006. https://doi.org/10.1088/0953-2048/28/10/104006.

[21] Suzuki K, Matsuda J, Yoshizumi M, Izumi T, Shiohara Y, Iwakuma M, et al. Development of a laser scribing process of coated conductors for the reduction of AC losses. Superconductor

Science and Technology 2007;20(8);822–6. https://doi.org/10.1088/0953-2048/20/8/017.

[22] Nast R, Vojenčiak M, Demencik E, Kario A, Ringsdorf B, Jung A, et al. Influence of laser striations on the properties of coated conductors. Journal of Physics: Conference Series 2014;507(2);022023. https://doi.org/10.1088/1742-6596/507/2/022023.

[23] N. Amemiya, Y. Sogabe, M. Shigemasa, H. Uegaki and S. Sonobe. SCSC-IFB cable: a novel low-AC-loss cable composed of multifilament coated conductors with superconducting inter-filament bridges. Superconductor Science and Technology 2026;39;045010. https://doi.org/10.1088/1361-6668/ae54d7.

[24] Cai X, Kesgin I, Schmidt R, Chen Y and Selvamanickam V. Completely etch-free fabrication of multifilamentary coated conductor using inkjet printing and electrodeposition. IEEE Transactions on Applied Superconductivity 2013;23(3);6603005. https://doi.org/10.1109/TASC.2013.2244638.

[25] Duckworth RC, List FA, Paranthaman MP, Rupich MW, Zhang W, Xie YY, et al. Low ac loss geometries in YBCO coated conductors. Physica. Part C 2007;463–465;755–60. https://doi.org/10.1016/j.physc.2007.03.499.

[26] Duckworth RC, Paranthaman MP, Bhuiyan MS, List FA, Gouge MJ and Losses AC. AC losses in YBCO coated conductor with inkjet filaments. In: IEEE Transactions on Applied Superconductivity 2007;17(2);3159–62. https://doi.org/10.1109/TASC.2007.897989.

[27] Hopkins SC, Mitchell-Williams TB, Vanden Bussche DRV, Calleja A, Vlad VR, Vilardell M, et al. Low AC Loss inkjet-printed multifilamentary YBCO coated conductors. IEEE Transactions on Applied Superconductivity 2016;26(3);1–5. https://doi.org/10.1109/TASC.2016.2542001.

[28] Lam SKH and Sankrithyan B. B. Sankrithyan, HTSC devices fabricated by selective epitaxial growth. Superconductor Science and Technology 1999;12(4);215–8. https://doi.org/10.1088/0953-2048/12/4/007.

[29] Kopera Ľ, Šmatko V, Prusseit W, Polák M, Semerad R, Štrbík V, et al. In situ patterning of filamentary YBCO coated conductors. Physica. Part C 2008;468(24);2351–5. https://doi.org/10.1016/j.physc.2008.08.013.

[30] Matsumoto A, Tachiki M and Ooi S. Development of YBCO patterned multi-filamentary film using photolithography method. IEEE Transactions on Applied Superconductivity 2023;33(5);1–4. https://doi.org/10.1109/TASC.2023.3244515.

[31] Fujimoto H, Matsumoto A, Ooi S, Tachiki M, Inoue M and Teranishi R. Consideration of magnetic flux distribution in multi−filamented $YBa_2Cu_3O_{7-\delta}$ films by controlling crystal array using surface−modified substrate. IEEE Transactions on Applied Superconductivity 2024;34(3);1–4. https://doi.org/10.1109/TASC.2024.3362729.

[32] Matsumoto A, Tachiki M, Ooi S, Teranishi R and Inoue M. Microstructural study of YBCO thin films with stripe-patterned substrates for ultra-fine multi-filaments. IEEE Transactions on Applied Superconductivity 2024;34(3);1–4. https://doi.org/10.1109/TASC.2024.3366159.

[33] Wada T, Fujimoto H, Kawahara Y, Matsumoto A, Ooi S, Tachiki M, et al. Cross-sectional microstructure observation of $YBa_2Cu_3O_{7-\delta}$ multifilament films fabricated on Nb stripes. Materials Today Communications 2026;50;114552. https://doi.org/10.1016/j.mtcomm.2025.114552.

[34] Harriott LR. Limits of lithography. Proceedings of the IEEE 2001;89(3);366–74. 10.1109/5.915379.

[35] Fan HJ, Gösele U and Zacharias M. Formation of nanotubes and hollow nanoparticles based on Kirkendall and diffusion processes: A review. Small 2007;3(10);1660–71. 10.1002/smll.200700382.//.

[36] K. Konya, K. Ootaguro, T. Nishiyama, R. Teranishi, T. Kiss, K. Yamada, K. Kaneko, M. Yoshizumi, T. Izumi Effect of holding temperature on microstructures and Jc properties of

YBa2Cu3O7-X films fabricated by TFA-MOD method. Physica C: Superconductivity and its Applications 2013;494
https://doi.org/10.1016/j.physc.2013.04.067

[37] T. Izumi and K. Nakaoka, Control of artificial pinning centers in REBCO coated conductors derived from the trifluoroacetate metal-organic deposition processSupercond. Sci. Technol. 2017;31(3);034008.10.1088/1361-6668/aa9dd2

[38] Jain A, Ong SP, Hautier G, Chen W, Richards WD, Dacek S, et al. Commentary: The Materials Project: A materials genome approach to accelerating materials innovation. APL Materials 2013;1(1);011002. https://doi.org/10.1063/1.4812323.

[39] Materials data on $Ba_5Nb_4O_{15}$ by materials project. United States. N & P 2020. [Cited on 15 Jan 2026]. Available from: https://doi.org/10.17188/1207019.

[40] Materials Data on CuO by Materials Project. United States. N & P 2020. [Cited on 15 Jan 2026]. Available from: https://doi.org/10.17188/1285757.

[41] Materials data on Y2Cu2O5 by materials project. United States. N & P 2020. [Cited on 15 Jan 2026]. Available from: https://doi.org/10.17188/1202869.

Table 1. Stripe widths and heights measured by laser microscopy.

*Note: These values are representative measurements obtained from typical regions after confirming the overall morphological uniformity across the sample via low-magnification observation.

	Nb-1	Nb-2	Nb-5	Nb-10
Stripe widths (μm)	3.4	4.9	8.0	13.1
Stripe heights (μm)	0.075	0.12	0.18	0.20

Table 2. Heights of the stripe, thin films on the stripe, and YBCO thin films after heat treatment, for various samples.

*Note: These values are local measurements obtained from a single representative cross-section, which was carefully selected based on the typical morphology confirmed by low-magnification SEM.

	Nb-1	Nb-2	Nb-5	Nb-10
Stripe heights (μm)	0.39	0.67	1.04	1.50
Heights of thin film on the stripe (μm)	0.28	0.26	0.29	0.37
Heights of YBCO thin film (μm)	0.51	0.52	0.39	0.50

Table 3. Estimated volumes of the non-superconducting phases derived from the volume of $Ba_5Nb_4O_{15}$ (TEM specimens have a thickness of 100 nm).

	Nb-2	Nb-5	Nb-10
Measured volume of $Ba_5Nb_4O_{15}$ (μm^3)	0.199	0.508	0.975
Est. volume of $Y_2Cu_2O_5$ (μm^3)	0.0857	0.219	0.420
Est. volume of CuO (μm^3)	0.0626	0.160	0.307
Est. total volume of non-superconducting phases (μm^3)	0.148	0.379	0.727
Measured volume of non-superconducting phases (μm^3)	0.133	0.316	0.623

Table 4. Comparison of representative multifilamentation techniques for REBCO coated conductors.

Method	Principle	Typical gap width	Thermal damage	Main advantage	Main limitation	References
Laser scribing	Top-down	16.2 µm [ref.23]	Yes	Mature and simple process	Heat-affected zone	[14–23]
Inkjet printing	Bottom-up	150 µm [ref.24]	No	No thermal damage	Wide gap due to ink spreading	[24–27]
Present work	Bottom-up photolitho graphy	4.9 µm [This work]	No	Narrow continuous gap layer	Lithographic process required	[30–33]

Figure Captions

Figure 1. Schematic of the photolithographic patterning process and the fabricated substrate with four Nb stripes.

Figure 2. Thermal history of YBCO film growth [36,37].

Figure 3. Laser micrographs and height profiles of the Nb stripes patterned on a single STO substrate: (a) Nb-1, (b) Nb-2, (c) Nb-5, and (d) Nb-10.

Figure 4. X-ray diffraction (XRD) θ-2θ results of YBCO thin films (a) without and (b) with Nb stripes (reproduced from our previous work [33]).

Figure 5. Secondary-electron- scanning electron microscopy (SE-SEM) micrographs of YBCO thin films with Nb stripes of the (a) Nb-1, (b) Nb-2, (c) Nb-5, and (d) Nb-10.

Figure 6. Element maps of YBCO thin films with Nb stripe (a) Nb-1, (b) Nb-2, (c) Nb-5, and (d) Nb-10.

Figure 7. Cross-sectional High-angle annular dark-field-scanning transmission electron microscopy (HAADF-STEM) images of YBCO thin films with Nb stripe of the (a) Nb-1, (b) Nb-2, (c) Nb-5, and (d) Nb-10 samples. (Nb-1 and Nb-10 micrographs were reproduced from our previous work [33]).

Figure 8. STEM-EDS element maps of YBCO thin films with Nb stripe of the Nb-1, (b) Nb-2, (c) Nb-5, and (d) Nb-10.

Figure 9. (a) Bright-field- Transmission electron microscopy (BF-TEM) images and (b) selected-area electron diffraction pattern (SAEDp) of the regions indicated by the red circles in the BF-TEM images.

Figure 10. MO image of a YBCO thin film with stripes at 10 K under 40 Oe.

Figure1

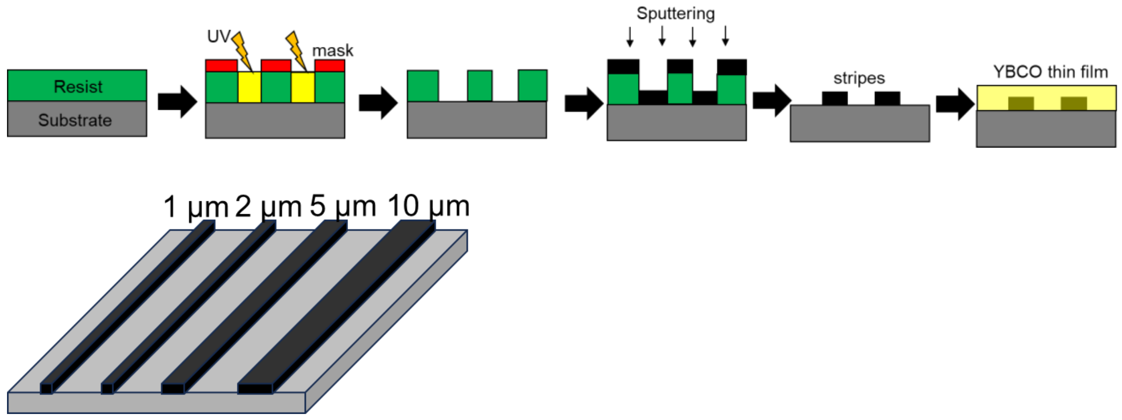
Resist
Substrate
UV
mask
Sputtering
stripes
YBCO thin film
1 µm 2 µm 5 µm 10 µm

Figure2

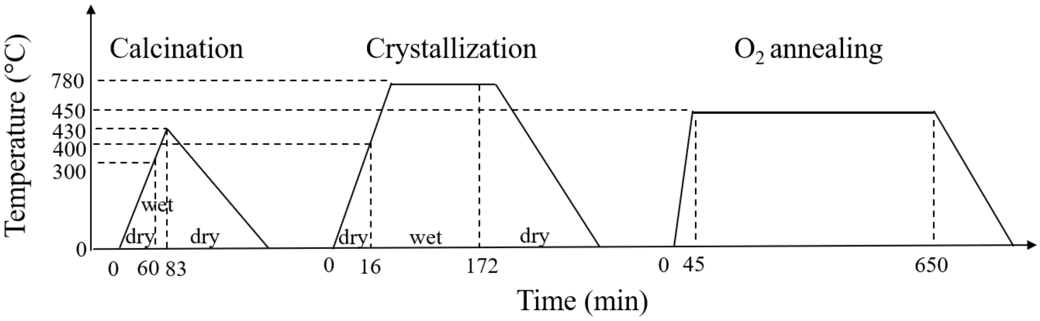

Calcination
Crystallization
O2 annealing
Temperature (°C)
780
450
430
400
300
0
wet
dry
dry
dry
wet
dry
0
60
83
0
16
172
0
45
650
Time (min)

Figure3

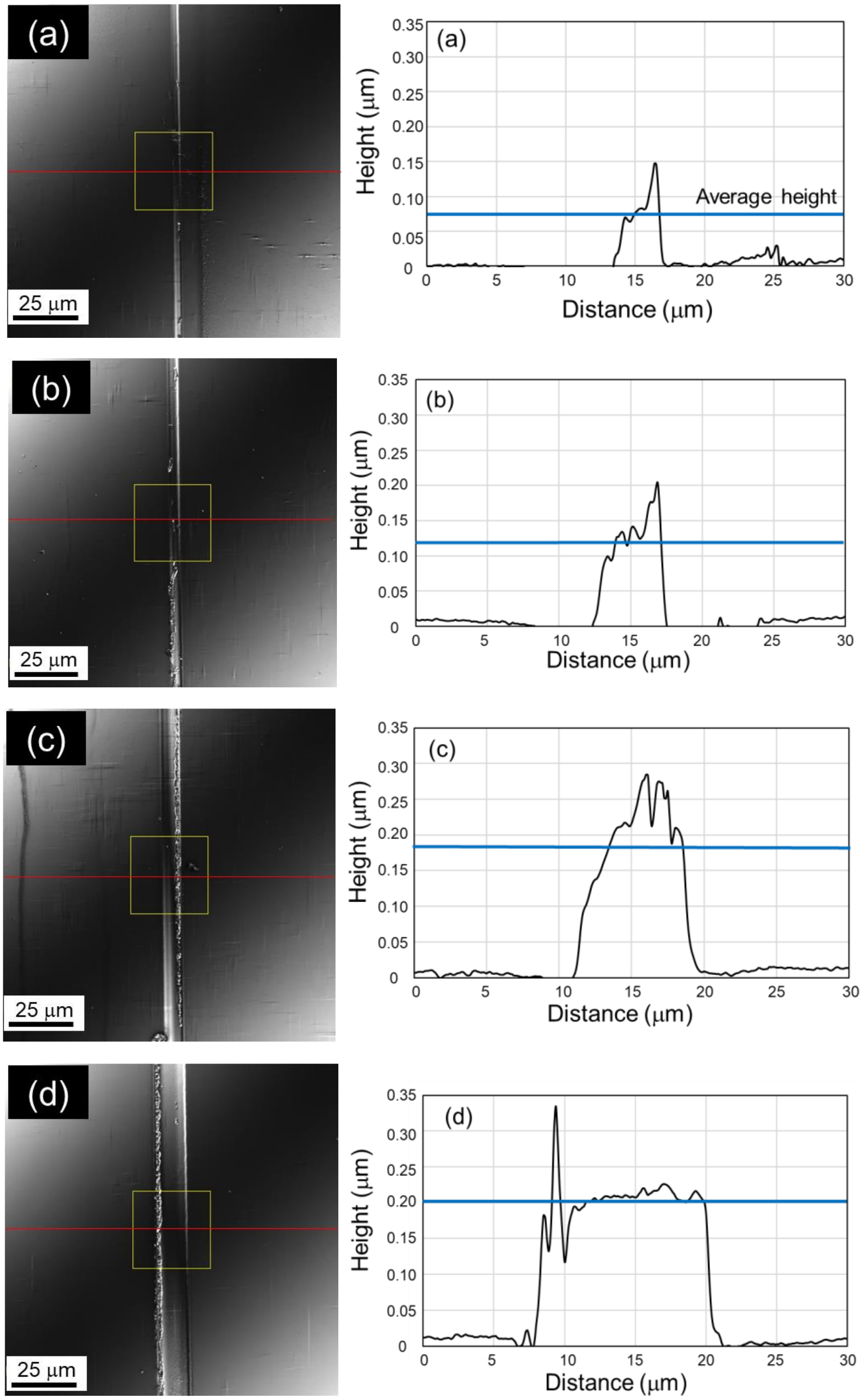
(a)
25 μm
(b)
25 μm
(c)
25 μm
(d)
25 μm
Average height
Height (μm)
Distance (μm)
0
0.05
0.10
0.15
0.20
0.25
0.30
0.35
0
5
10
15
20
25
30

Figure4

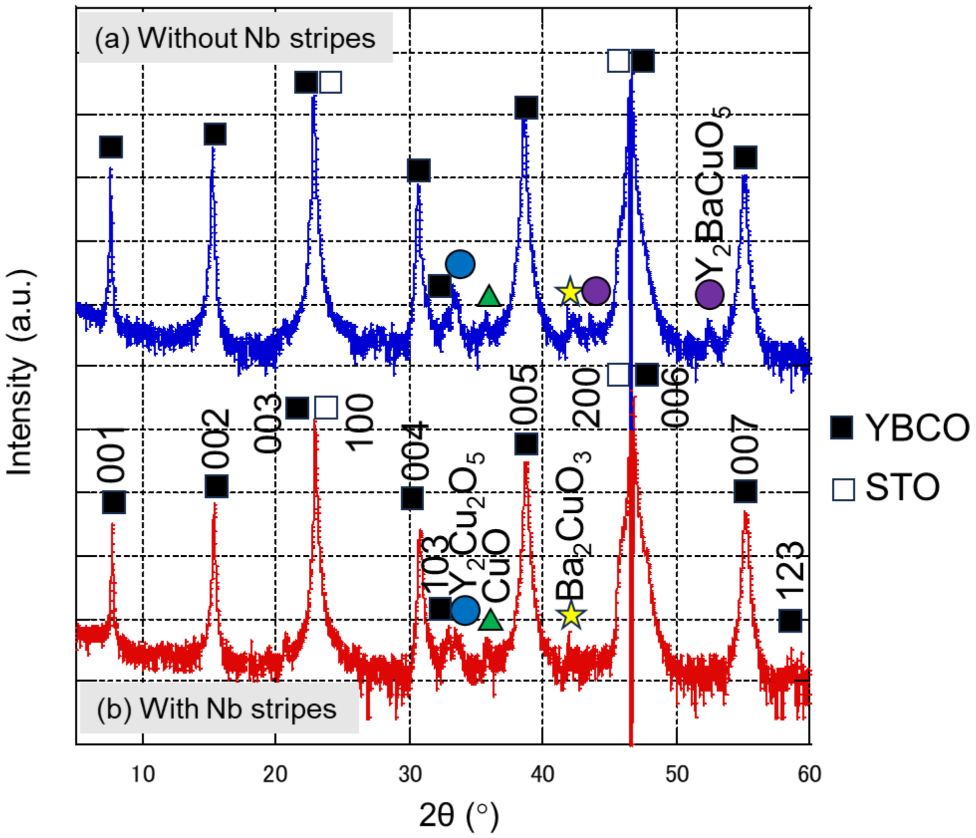

(a) Without Nb stripes
(b) With Nb stripes
Intensity (a.u.)
2θ (°)
10
20
30
40
50
60
001
002
003
100
004
103
005
200
006
007
123
$Y_2Cu_2O_5$
CuO
Ba_2CuO_3
Y_2BaCuO_5
YBCO
STO

Figure5

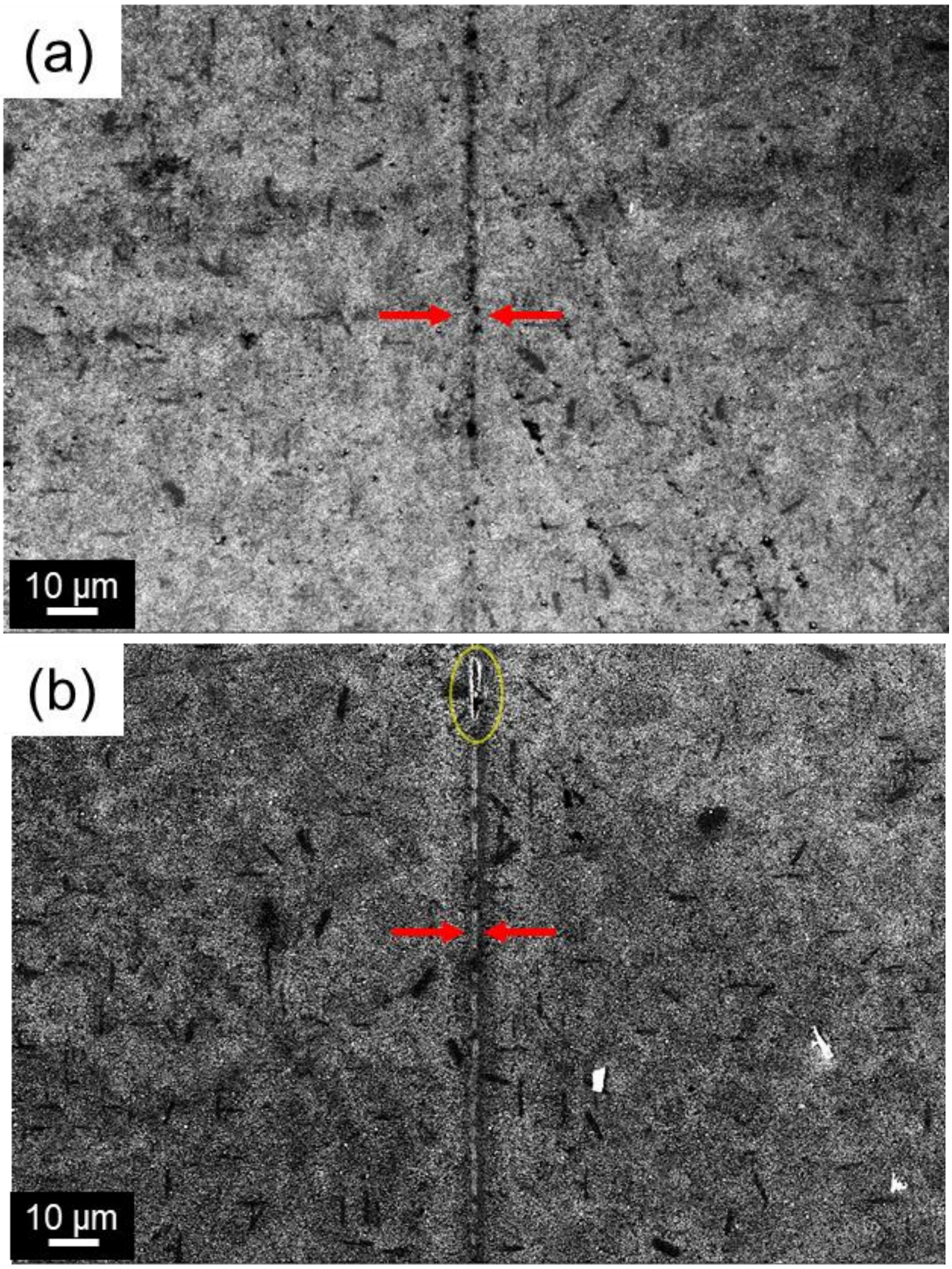

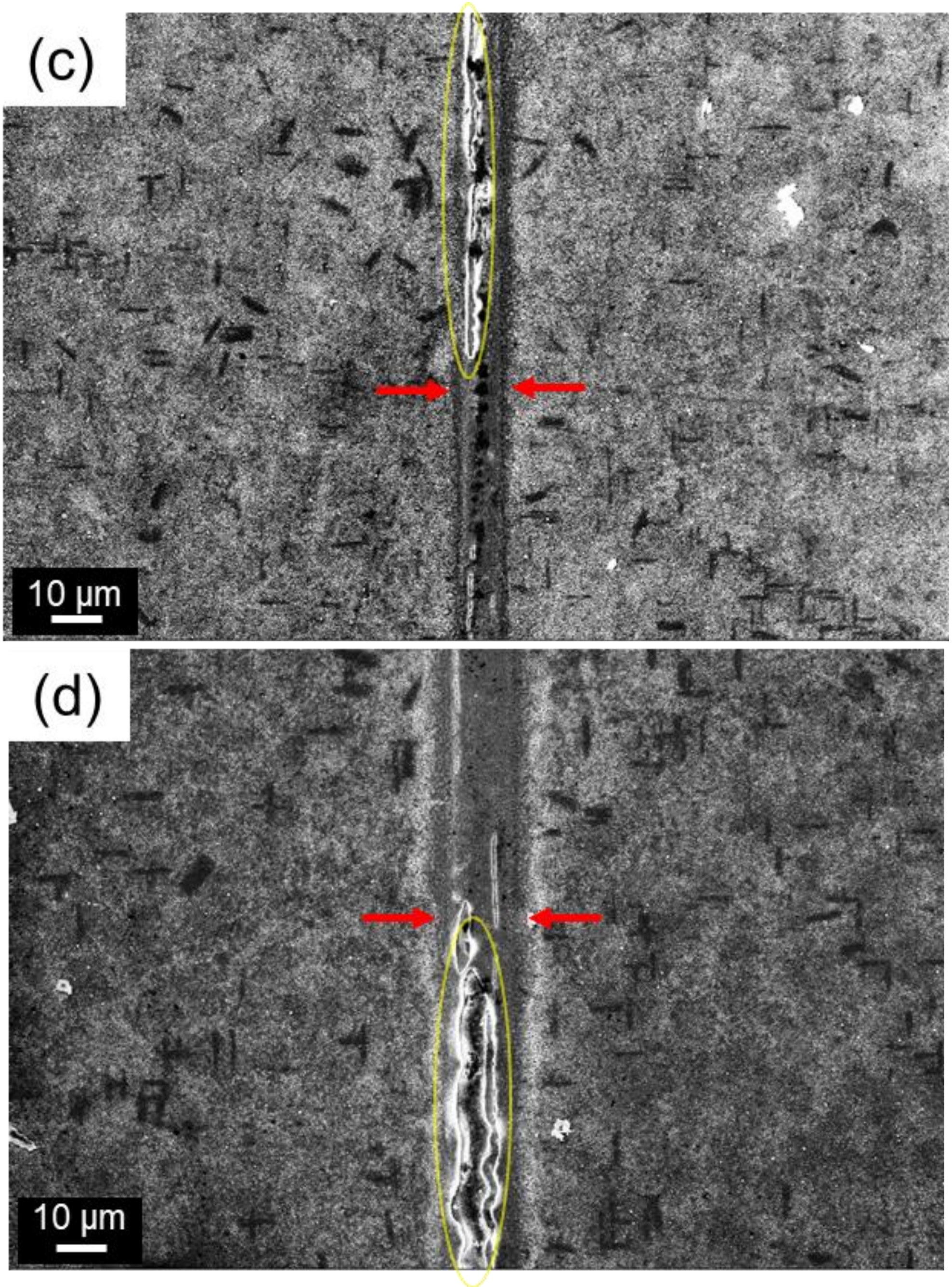
(c)
10 μm
(d)
10 μm

Figure6

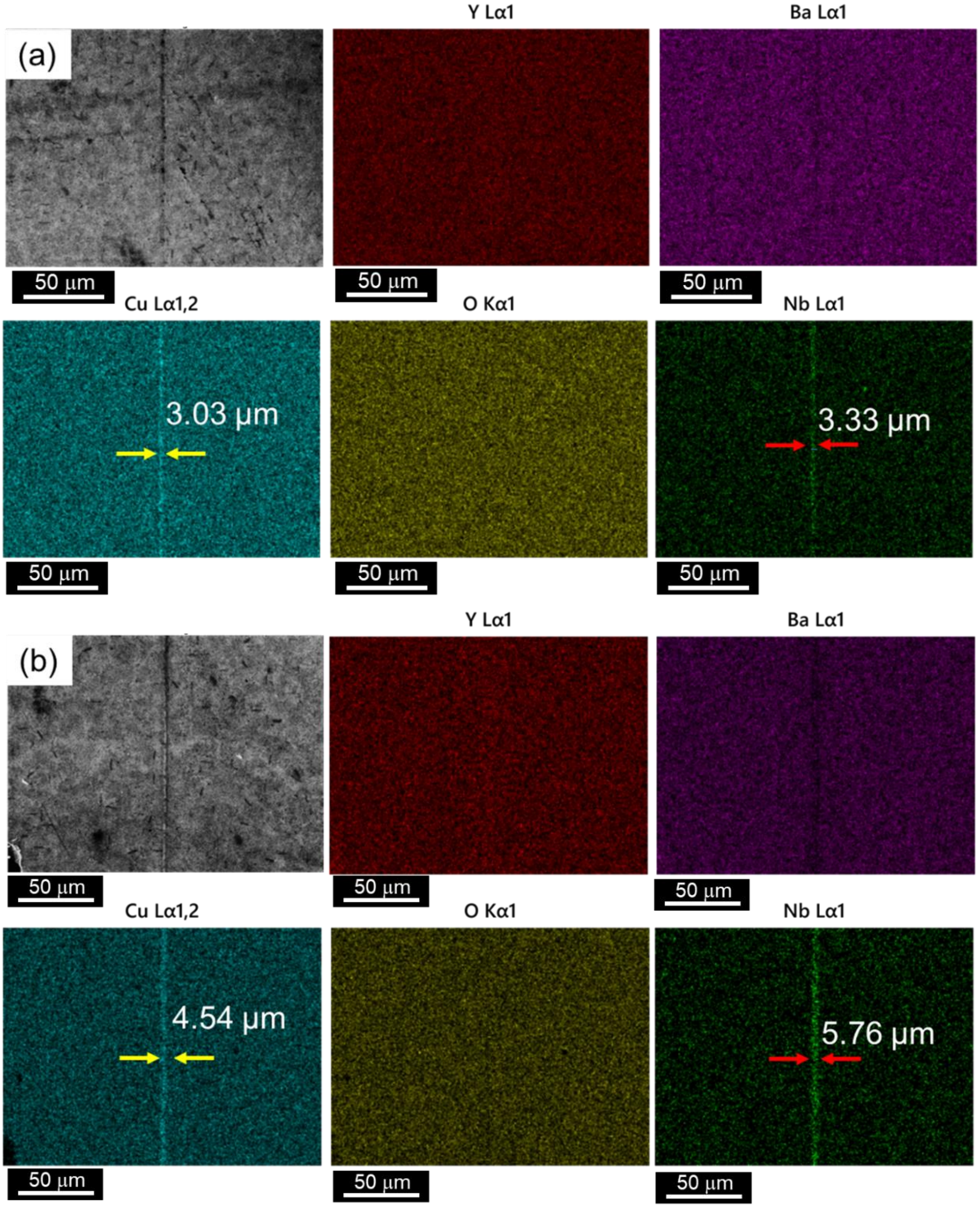

(a)
Y Lα1
Ba Lα1
Cu Lα1,2
O Kα1
Nb Lα1
3.03 μm
3.33 μm
50 μm
(b)
Y Lα1
Ba Lα1
Cu Lα1,2
O Kα1
Nb Lα1
4.54 μm
5.76 μm
50 μm

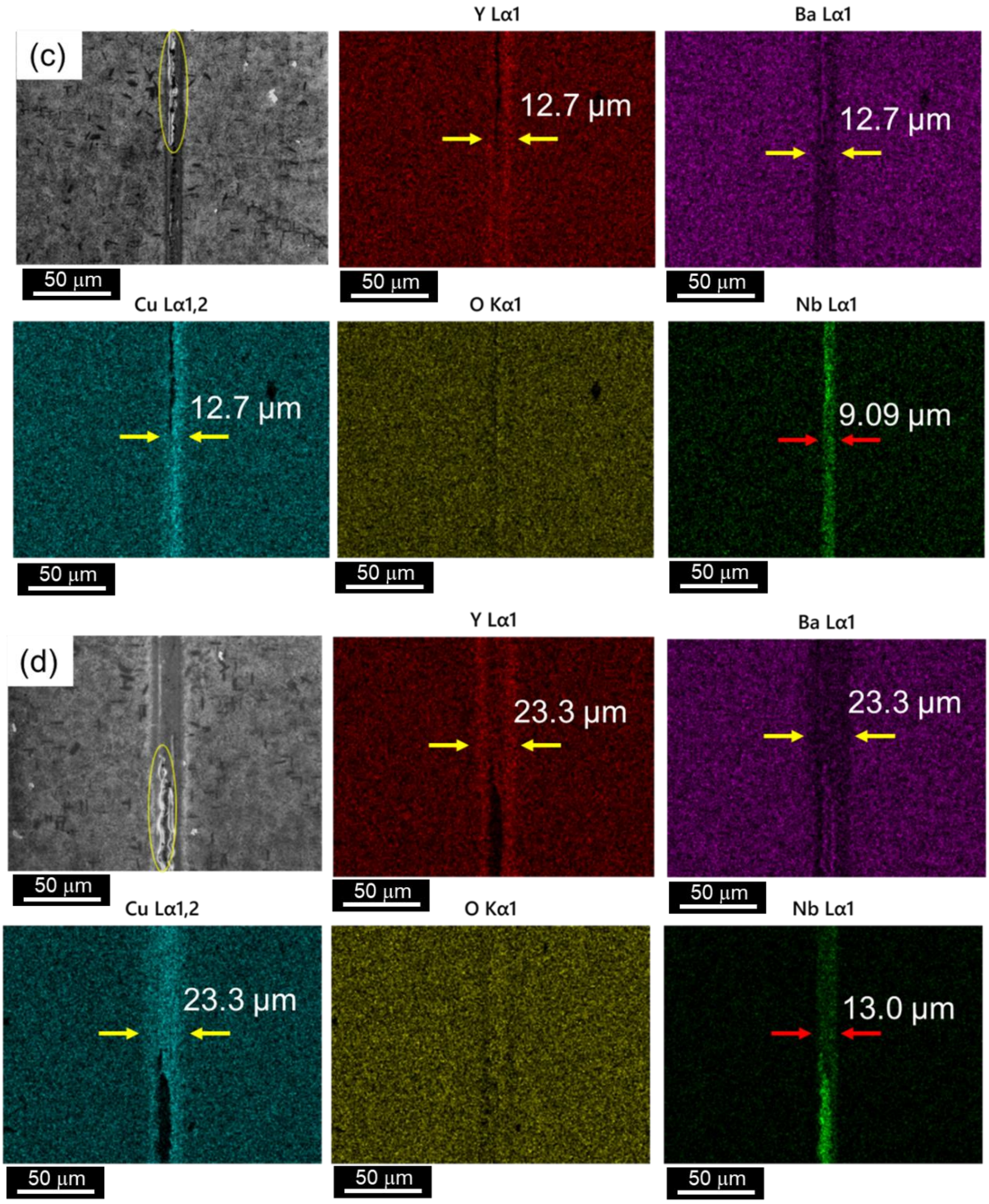

(c)
Y Lα1
Ba Lα1
12.7 μm
12.7 μm
50 μm
50 μm
50 μm
Cu Lα1,2
O Kα1
Nb Lα1
12.7 μm
9.09 μm
50 μm
50 μm
50 μm
(d)
Y Lα1
Ba Lα1
23.3 μm
23.3 μm
50 μm
50 μm
50 μm
Cu Lα1,2
O Kα1
Nb Lα1
23.3 μm
13.0 μm
50 μm
50 μm
50 μm

Figure7

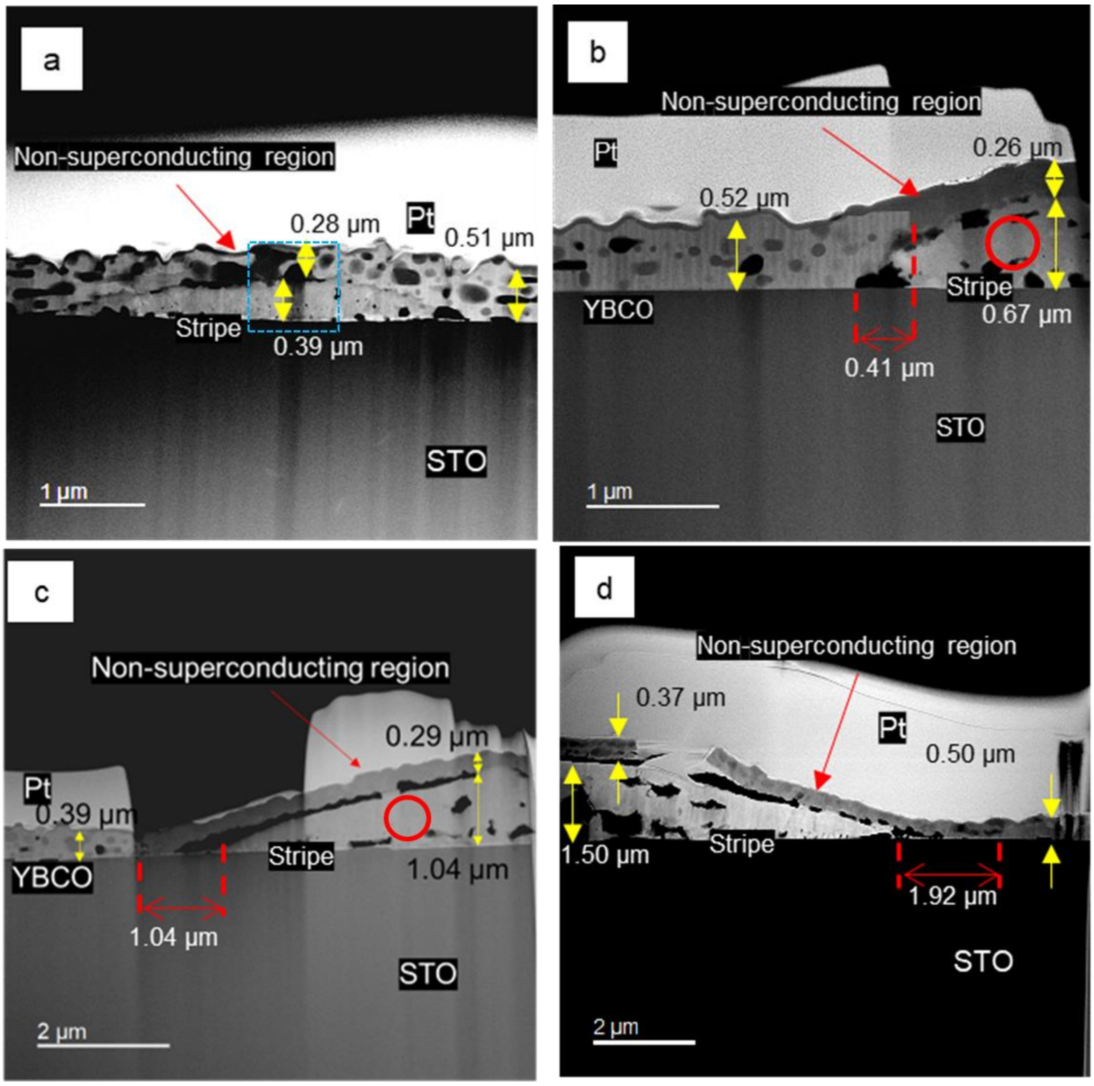
a
Non-superconducting region
0.28 μm
Pt
0.51 μm
Stripe
0.39 μm
STO
1 μm
b
Non-superconducting region
Pt
0.26 μm
0.52 μm
Stripe
YBCO
0.67 μm
0.41 μm
STO
1 μm
c
Non-superconducting region
0.29 μm
Pt
0.39 μm
Stripe
YBCO
1.04 μm
1.04 μm
STO
2 μm
d
Non-superconducting region
0.37 μm
Pt
0.50 μm
1.50 μm
Stripe
1.92 μm
STO
2 μm

Figure8

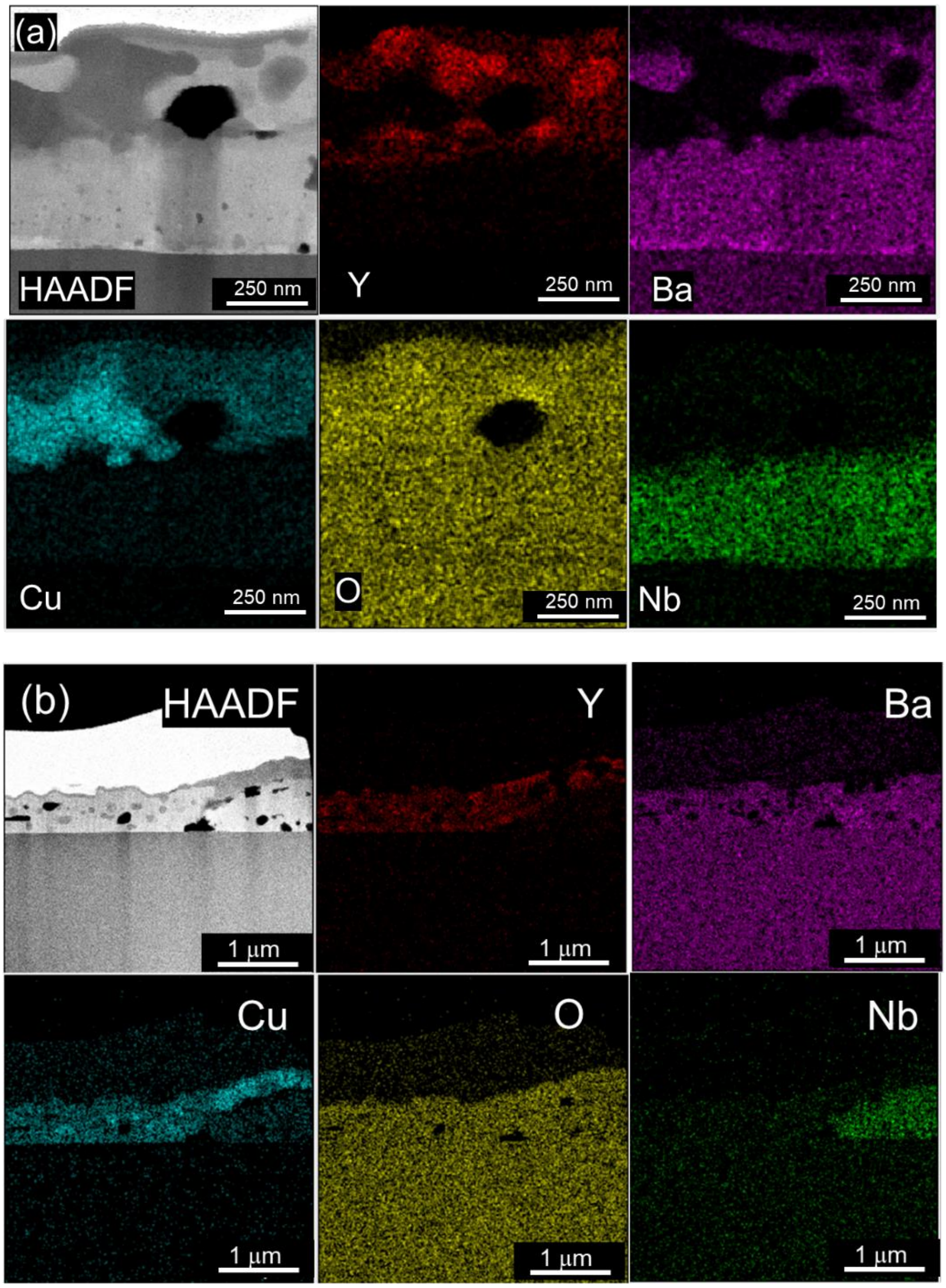
(a)
HAADF
250 nm
Y
250 nm
Ba
250 nm
Cu
250 nm
O
250 nm
Nb
250 nm
(b)
HAADF
1 μm
Y
1 μm
Ba
1 μm
Cu
1 μm
O
1 μm
Nb
1 μm

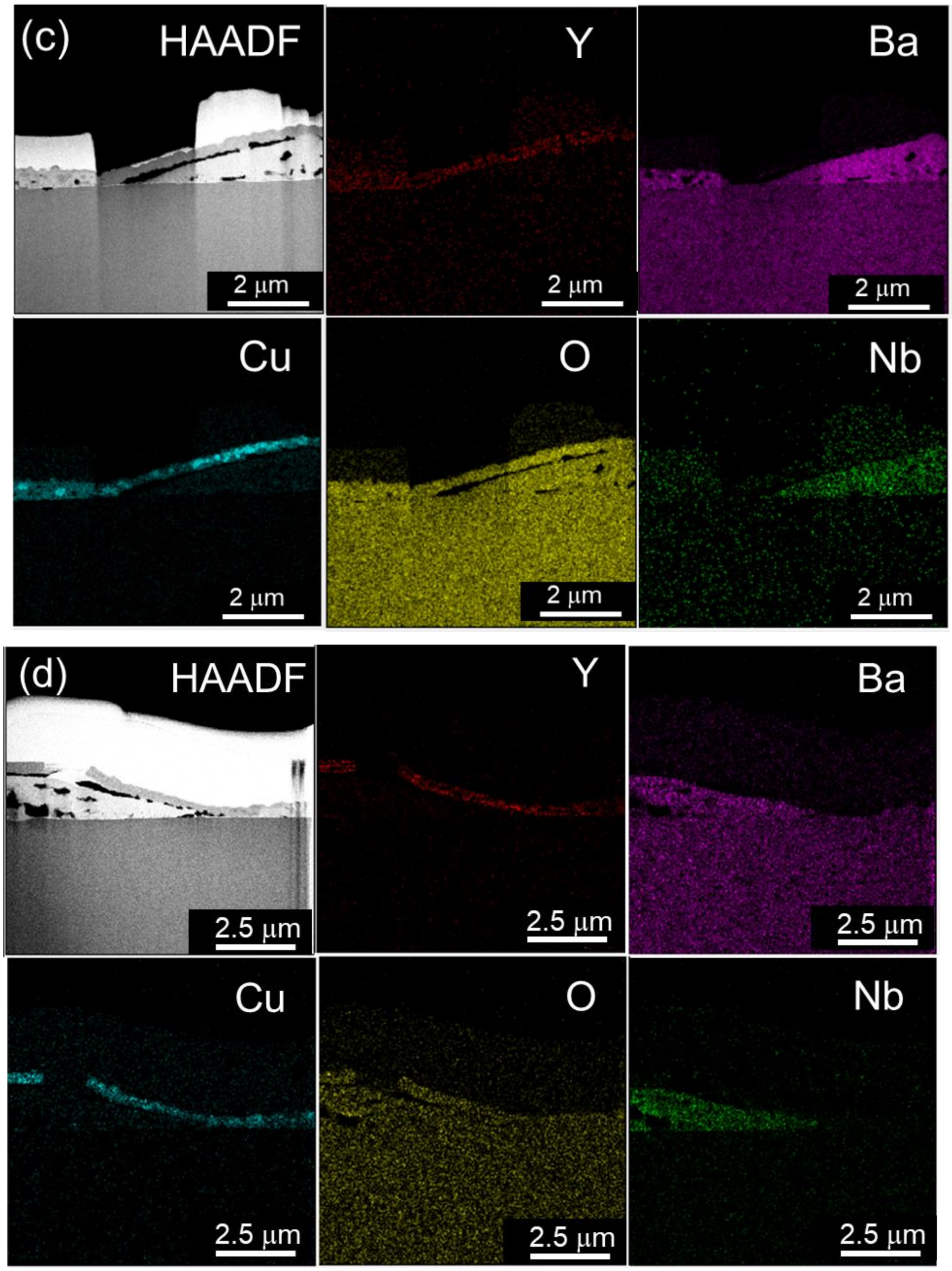

(c)
HAADF
2 μm
Y
2 μm
Ba
2 μm
Cu
2 μm
O
2 μm
Nb
2 μm
(d)
HAADF
2.5 μm
Y
2.5 μm
Ba
2.5 μm
Cu
2.5 μm
O
2.5 μm
Nb
2.5 μm

Figure9

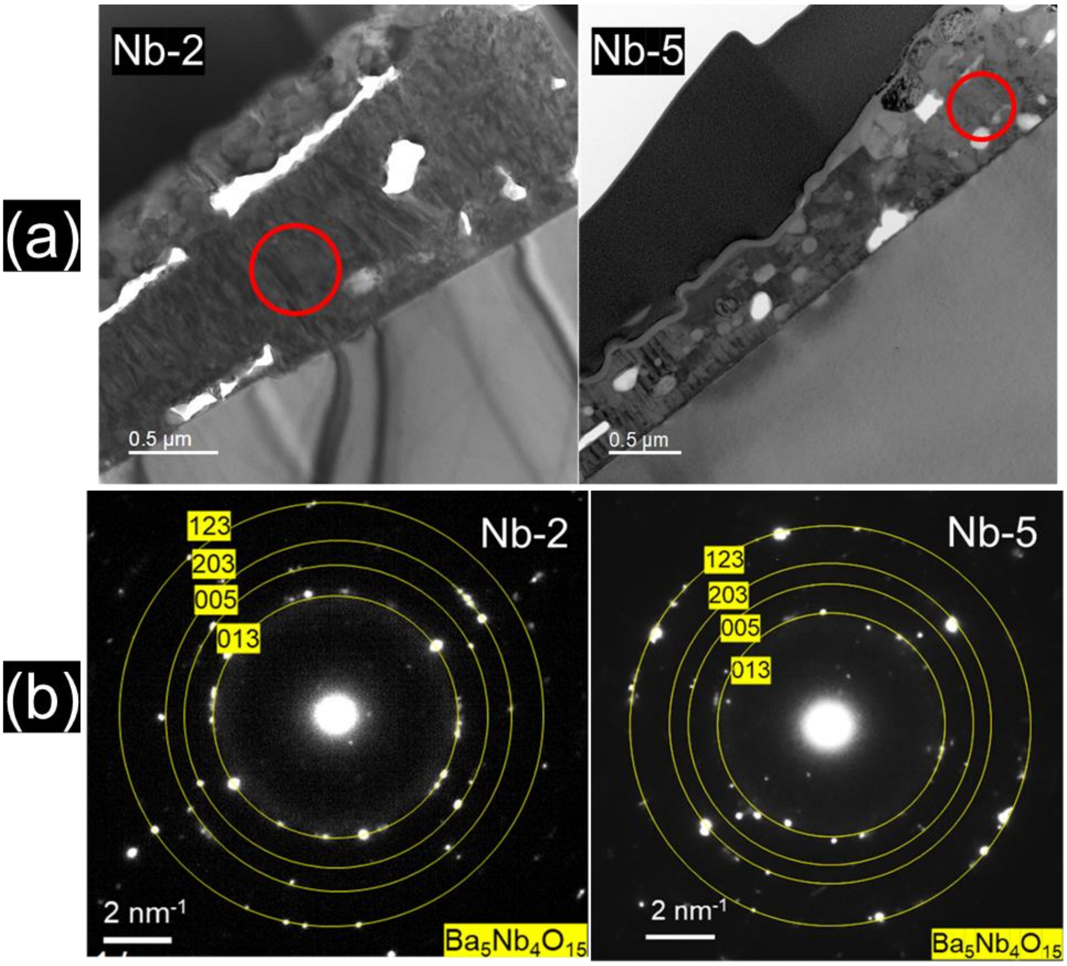

(a)
Nb-2
0.5 μm
Nb-5
0.5 μm
(b)
Nb-2
123
203
005
013
2 nm-1
Ba5Nb4O15
Nb-5
123
203
005
013
2 nm-1
Ba5Nb4O15

Figure10

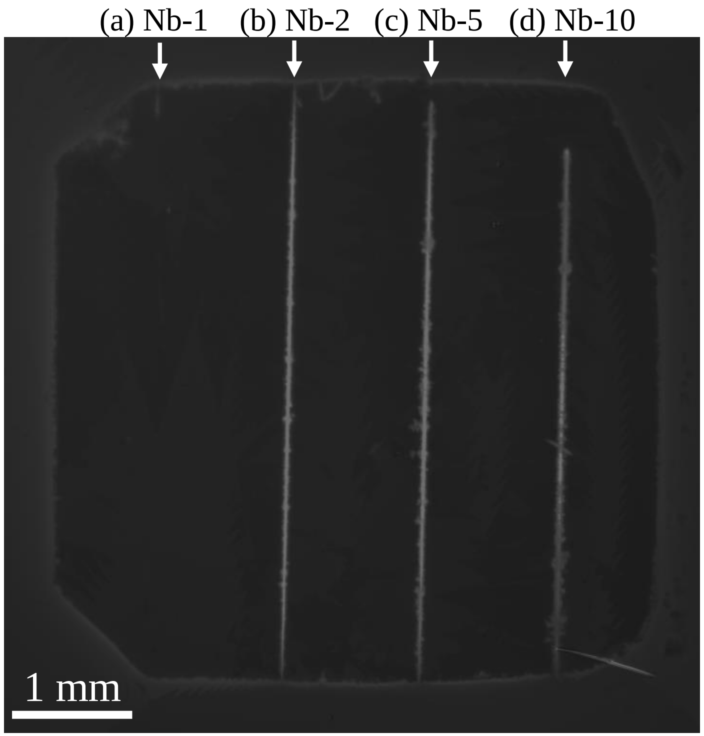

Graphical abstract_revised

Stripe-Width-Dependent Microstructural Evolution in Multifilamented $YBa_2Cu_3O_{7-\delta}$ Films Revealed by Cross-Sectional Analysis

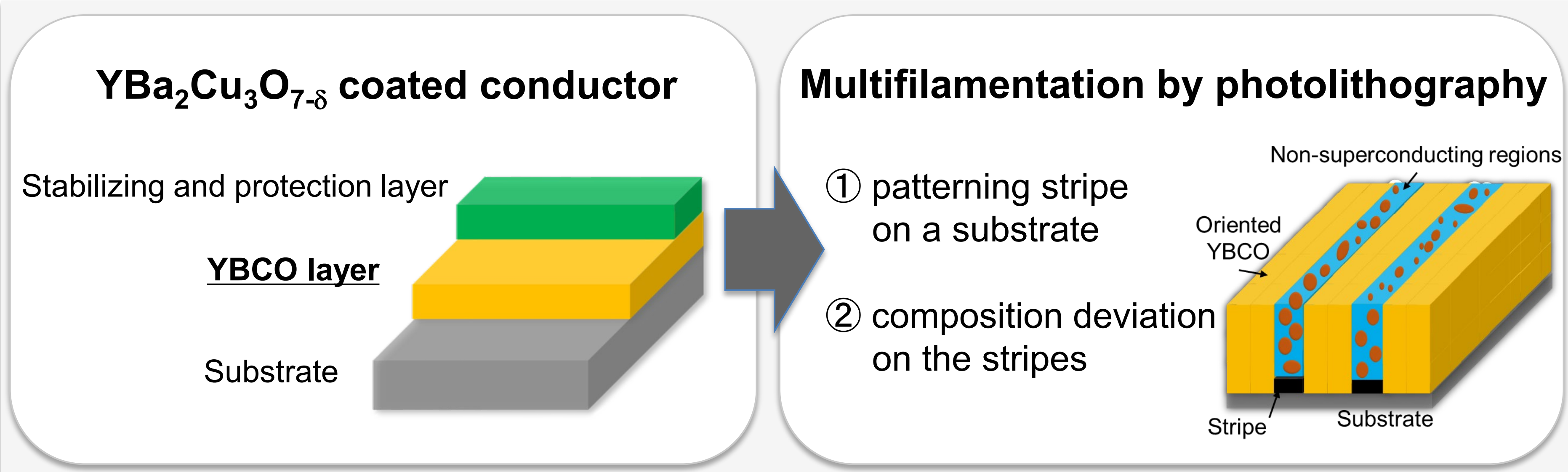

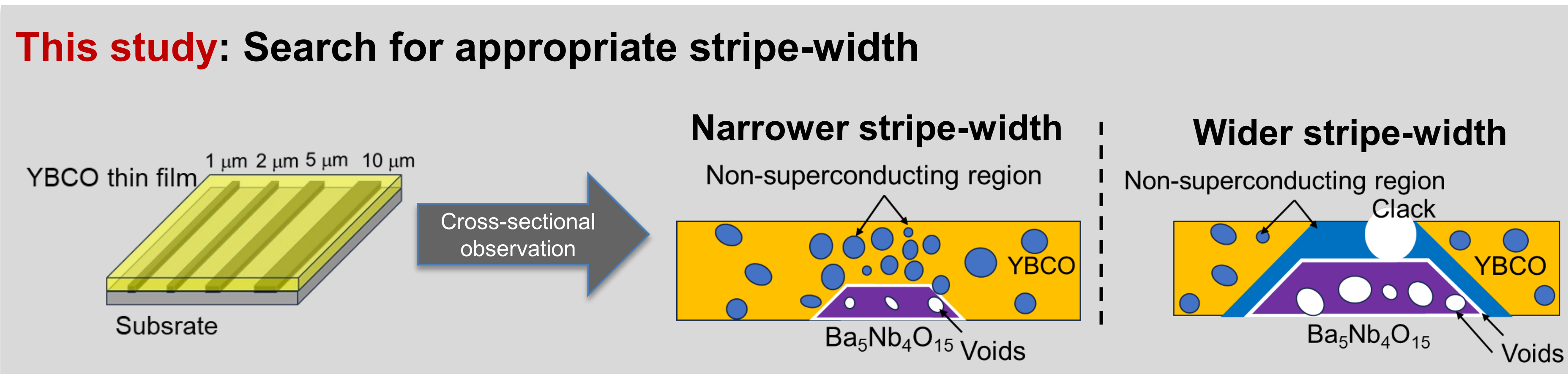

Conclusion

These results indicate that an optimal stripe width exists to achieve a continuous and narrow non-superconducting region.